Cation-Disorder-Enhanced Unintentional Doping in MgSnN$_2$

Feng Ning,[1,2] Jing Huang,[1] and Jun Kang [1,*]

[1]*Beijing Computational Science Research Center, Beijing 100193, China*
[2]*School of Physics and Electronics, Nanning Normal University, Nanning 530001, China*

MgSnN$_2$ has recently attracted significant interest as a promising candidate for applications in green light-emitting diodes and photovoltaic absorbers. However, the experimentally synthesized MgSnN$_2$ samples suffer from a high concentration of unintentionally doped electrons, and their origin is not fully understood yet. By performing first-principles calculations, we investigate the properties of intrinsic point defects and oxygen impurities in cation-ordered and -disordered wurtzite MgSnN$_2$. It is found that the cation antisite defect Sn$_{Mg}$ is the predominant donor defect, contributing an electron concentration as high as 10^{17} cm^{-3} to cation-ordered MgSnN$_2$. However, this value is 2–3 orders of magnitude lower than experimental observations ($10^{19} - 10^{20}$ cm^{-3}). We further show that cation disorder significantly decreases the formation energies of defects, leading to a much higher electron concentration (10^{19} cm^{-3}) than in the case of the cation-ordered phase. The reduced formation energy can be understood by the energy gain due to the creation of energetically favorable local motif structures after the formation of defects. Hence, reducing the degree of cation disorder is beneficial for decreasing the densities of defects and self-doped carriers.

I. INTRODUCTION

The III-N semiconductors and related alloys, such as GaN, AlN, In$_x$Ga$_{1-x}$N, and Al$_x$Ga$_{1-x}$N, have been extensively studied and found wide application in optoelectronic devices. They are the active materials for short-wavelength light-emitting diodes (LEDs) [1], power electronics [2], and photovoltaic absorbers [3]. However, there remain several challenges for further improvements in the cost-to-efficiency ratio of these applications, such as the high cost of the elements (especially indium and gallium) [4,5], weak green-light emission intensity [6], and the difficulty of high-quality epitaxial growth on heterostructures [7,8]. Recently, II-IV-N$_2$ semiconductors have attracted much attention as alternatives to the III-N semiconductors in optoelectronic applications [9]. The wurtzite II-IV-N$_2$ semiconductors are structural analogs to III-V materials formed by substituting the group-III cations with group-II and group-IV elements. They are expected to enhance the functionality of optoelectronic devices by tuning their ternary chemistry and the degree of cation disorder [4,9–11]. Motivated by their distinctive properties, many investigations focus on studying II-IV-N$_2$ semiconductors, such as ZnSiN$_2$, ZnGeN$_2$, ZnSnN$_2$, and MgSnN$_2$ [12–15]. In

particular, MgSnN$_2$, with a band gap of 2.3 eV, which is favorable for filling the "green gap" in nitride-based LEDs, was successfully synthesized recently [4,5,7,9,16–18]. Moreover, the band structure of MgSnN$_2$ can be effectively tuned by various phase structures, stoichiometry, and cation disorder [17,19,20]. Highly tunable electronic properties make MgSnN$_2$ a promising candidate for application in green LEDs, tandem solar cells, and other optoelectronic devices.

Despite many advantages, a major problem preventing the practical application of MgSnN$_2$ is the high concentration of unintentionally doped electrons in the experimentally synthesized samples [16,19], which can be up to 10^{19}–10^{20} cm^{-3}. This concentration of carriers exceeds the ideal range (10^{16}–10^{18} cm^{-3}) for photovoltaic applications [21,22]. Moreover, a high electron-carrier concentration causes the Burstein-Moss effect, leading to a large optical gap [19,23,24]. In addition, devices with a high concentration of unintentionally doped carriers exhibit reduced mobility due to strong ionized-impurity scattering [17,19]. To date, the source of such a high electron concentration is not fully understood yet. Han *et al.* theoretically studied the properties of native defects and oxygen impurities in cation-ordered MgSnN$_2$ [22]. They found that the Sn-on-Mg substitution could lead to self-doped *n*-type conductivity, in qualitative agreement with experiments. However, according to their calculations, the concentration of self-doped electrons induced by native defects and impurities

---

*jkang@csrc.ac.cn

is 2–3 orders of magnitude lower than the experimentally measured values. Therefore, to control the carrier density in MgSnN$_2$ and promote its applications, further exploration of the origin of the high unintentional-doping level is highly desirable.

Han *et al.* [22] studied the defect properties for single-crystal MgSnN$_2$ with an ordered cation arrangement. Nevertheless, both experimental and theoretical studies confirm that there can be II-IV cation exchange in II-IV-V$_2$ compounds, leading to compositional disorder in the cation sublattice. For example, Greenaway *et al.* reported the coexistence of cation disorder in the wurtzite MgSnN$_2$ film [16]. It is found that cation disorder plays an important role in tuning the optoelectronic properties of II-IV-V$_2$ compounds, such as band gap, doping, band offsets, and electron-transport properties [5,10,11]. Particularly, the band gaps can be decreased by up to 1 eV through controlling the degree of cation disorder [25–27]. The change in band gap will influence the carrier density, according to the Boltzmann distribution. Furthermore, cation disorder can change the coordination environment around the defect sites, leading to a distinct Coulomb interaction, local bonding, and local lattice relaxation with respect to the cation-ordered environment. These effects directly affect the formation energies of defects and modify the unintentional doping concentrations. However, the implications of cation disorder on the defect properties of MgSnN$_2$ remain unclear. With the presence of cation disorder, the defect-formation energy becomes site dependent due to different local environments [28,29]. The increased complexity also brings challenges for defect calculations, such as how to properly choose the reference host and how to conduct a statistical average.

Here, we study the properties of native point defects and oxygen impurities in cation-ordered and -disordered wurtzite MgSnN$_2$ by first-principles calculations. It is found that the cation antisite defect Sn$_{Mg}$ is the predominant donor defect, resulting in a maximum *n*-type self-doping level of 10^{17} cm^{-3} in cation-ordered MgSnN$_2$. Therefore, cation-ordered wurtzite MgSnN$_2$ can meet the requirements for the electron concentration for photovoltaic applications. However, we find that cation disorder significantly decreases the formation energies of defects, leading to a much higher density of self-doped electrons (10^{19} cm^{-3}) than in the case of a cation-ordered phase. The reduced formation energy can be understood by the energy gain due to the creation of energetically favorable local motif structures after the formation of defects. Hence, such cation-disorder-enhanced unintentional doping could be a possible origin of the high electron-carrier value (10^{19}–10^{20} cm^{-3}) observed in experiments. These

results could be helpful for carrier control in MgSnN$_2$ samples and their applications in electronic devices.

II. METHODS

All the calculations are carried out using the Vienna *ab initio* simulation package based on density-functional theory [30,31] and the projector-augmented-wave method [32]. The exchange-correlation energy is described by both the generalized-gradient approximation (GGA) of Perdew, Burke, and Ernzerhof (PBE) [33] and the Heyd-Scuseria-Ernzerhof (HSE06) hybrid functional with a standard mixing parameter of 25% [34]. MgSnN$_2$ has orthorhombic symmetry with the *Pna*2$_1$ space group, containing 16 atoms in the primitive unit cell. Defect calculations are performed on a $3 \times 3 \times 3$ supercell with 432 atoms. The plane-wave expansion of the energy cutoff is set to 400 eV. A $6 \times 5 \times 6$ Monkhorst-Pack *k*-point mesh [35] is applied for the primitive cell and a single Γ point for the defect supercell. All the atomic positions are fully optimized until the total energies converge to below 10^{-4} eV and the forces acting on atoms are less than 10^{-2} eV/Å. Spin polarization is considered in all calculations. For defect-formation-energy calculations, the defect supercells are relaxed using the PBE functional, and the total energy and electronic structures are calculated with the HSE06 functional.

The formation energy of a point defect is determined by [36]

$$\Delta H_f(\alpha, q) = E_{\text{tot}}(\alpha, q) - E_{\text{tot}}(\text{host}) + \sum_i n_i \mu_i$$
$$+ q(E_{\text{VBM}} + \varepsilon_F) + E_{\text{corr}}(\alpha, q),$$

where $E_{\text{tot}}(\alpha, q)$ and $E_{\text{tot}}(\text{host})$ are the total energies of the supercell with defect α in charge state q and the pristine bulk supercell, respectively. E_{VBM} is the valence-band maximum (VBM) of the pristine supercell structure, and ε_F is the Fermi energy level referenced to the VBM. n_i is the number of atoms of type i exchanged with the reservoirs during the formation of the defect, and μ_i is the chemical potential of i. $E_{\text{corr}}(\alpha, q)$ corresponds to the correction energy, which includes the level alignment and removes spurious electrostatic interactions between the charged defect, its periodic image, and the neutralizing background charge under periodic boundary conditions [37–39]. We use the correction scheme proposed by Freysoldt, Neugebauer, and Van de Walle [37,38]. When the formation energies of a defect in two charge states, q and q', are equal, namely, $\Delta H_f(\alpha, q) = \Delta H_f(\alpha, q')$, the thermodynamic charge-transition level can be determined by

$$\varepsilon(q/q') = \frac{[E_{\text{tot}}(\alpha, q) + E_{\text{corr}}(\alpha, q)] - [E_{\text{tot}}(\alpha, q') + E_{\text{corr}}(\alpha, q')]}{q' - q} - E_{\text{VBM}}.$$

The equilibrium defect and charge-carrier concentrations are determined through the solution of the self-consistent Fermi energy with the calculated defect-formation energies and the charge-neutrality condition [40,41].

To generate cation-disordered MgSnN$_2$ structures, we construct a cluster-expansion (CE) Hamiltonian using the ATAT code [42] and perform Metropolis Monte Carlo (MC) simulations with the 432-atom supercell. More details are given in the Supplemental Material [43].

III. RESULTS AND DISCUSSION

A. Bulk properties of MgSnN$_2$

The most stable cation-ordered MgSnN$_2$ crystal is in the wurtzitelike phase with the $Pna2_1$ space group [16], as shown in Fig. 1(a). Each Mg and Sn atom is surrounded by four nearest-neighbor N atoms, while each N atom is coordinated by two Mg atoms and two Sn atoms. As shown in Table S1 within the Supplemental Material [43], the lattice parameters optimized by using the HSE06 method are $a = 5.87$ Å, $b = 6.83$ Å, and $c = 5.43$ Å, which are slightly smaller than those obtained by the PBE method and agree with the results obtained using strongly constrained and appropriately normed meta-GGA [16]. The calculated band structures of MgSnN$_2$ using the PBE and HSE06 methods are displayed in Fig. 1(b). A direct band gap of 2.39 eV, which is obtained using the HSE06 method, is revealed in Fig. 1(b). It is similar to the experimental result of 2.30 eV [17] and previous theoretical results of 2.47 and 2.28 eV [16,44]. In contrast, the band gap of 1.04 eV calculated with the PBE method is seriously underestimated.

The atomic chemical potentials should be determined before calculating the point-defect formation energy. The regions of chemical potentials are constrained by the formation enthalpy, ΔH_f, of the host material and its competing phases. In our calculations, the chemical potential, μ_i, of constituent i is referenced to its pure elemental phase, i.e., $\mu_i = \Delta\mu_i + E_i$, where E_i is the atomic energy of bulk Mg ($P63/mmc$), bulk Sn ($Fd\bar{3}m$), or the N$_2$ molecule ($P4_2/mnm$). The experimentally stable crystal structures of Mg$_3$N$_2$ ($Ia\bar{3}$), and Sn$_3$N$_4$ ($Fd\bar{3}m$) are considered as competing phases. Under thermal equilibrium growth conditions, $\Delta\mu_i$ should satisfy the following constraints:

$$\Delta\mu_{Mg} + \Delta\mu_{Sn} + 2\Delta\mu_N = \Delta H_f\,(\text{MgSnN}_2),$$

$$3\Delta\mu_{Mg} + 2\Delta\mu_N \leq \Delta H_f\,(\text{Mg}_3\text{N}_2),$$

$$3\Delta\mu_{Sn} + 4\Delta\mu_N \leq \Delta H_f\,(\text{Sn}_3\text{N}_4).$$

In addition, to avoid the formation of elemental phases, it is often required that $\Delta\mu_i$ is smaller than 0. However, the growth of II-IV-N$_2$ compounds often employs an activated N source generated by passing N$_2$ through an electron-cyclotron-resonance plasma source. As a result, $\Delta\mu_N$ can become positive and be up to $+15k_BT/\text{N}_2$ [45,46], corresponding to about 0.5 eV/N at the 700-K growth temperature of MgSnN$_2$ [16]. Therefore, it is required that $\Delta\mu_{Mg} < 0$ eV, $\Delta\mu_{Sn} < 0$ eV, and $\Delta\mu_N < 0.5$ eV. We calculate ΔH_f for the host material and its competing phases using the HSE06 functional. Based on the above equations and inequalities, we can depict the chemical potential diagram of MgSnN$_2$ as that shown in Fig. 1(c), where $\Delta\mu_{Mg}$ and $\Delta\mu_{Sn}$ are chosen as independent variables. For oxygen impurities, we consider molecules of O$_2$, MgO, and SnO$_2$ as the possible constraining secondary phases.

B. Defects in cation-ordered MgSnN$_2$

Here, we calculate the defect properties of MgSnN$_2$ under four representative growth environments, which are labeled by points A (Sn rich and Mg rich), B (Sn poor and Mg moderate), C (Sn rich and Mg poor), and
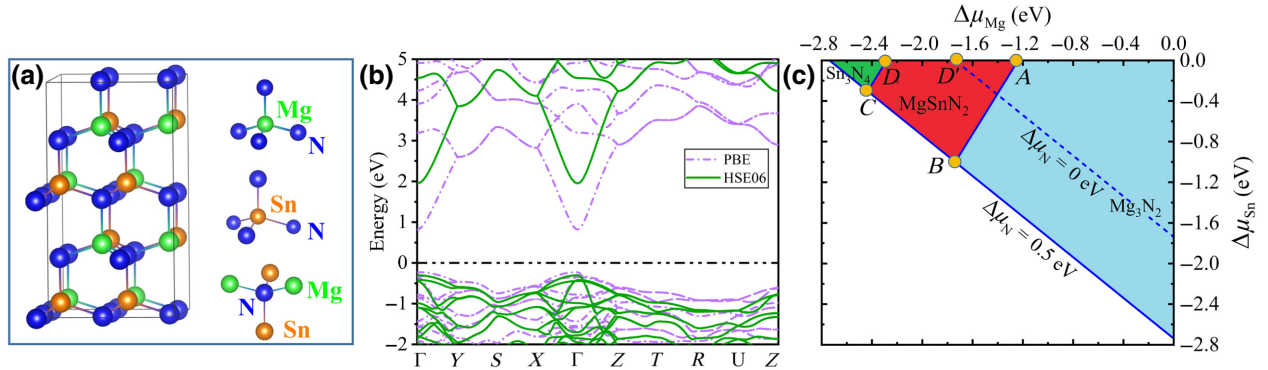

FIG. 1. (a) Conventional cell of cation-ordered MgSnN$_2$ with the $Pna2_1$ space group. (b) Band structures calculated using the PBE and HSE06 methods. (c) Chemical potential region (in red shadow) stabilizing MgSnN$_2$ with respect to binary competing phases with activated N source. Four distinct points, A, B, C, and D, are selected as the growth conditions for calculating defect-formation energies.

D (Sn rich and Mg poor) in Fig. 1(c). All the possible native point defects are considered, namely, vacancies (V_{Mg}, V_{Sn}, V_N), interstitials (Mg_i, Sn_i, N_i), and antisites (Mg_{Sn}, Mg_N, Sn_{Mg}, Sn_N, N_{Mg}, N_{Sn}). Since oxygen is a commonly observed impurity in nitrides, we also consider the O-on-N(O_N) substitutional defect. Figures 2(a)–2(d) show the formation energies of these defects with different charge states as a function of the Fermi level, and the corresponding charge-transition levels are presented in Fig. 2(e). It is seen that the formation energy of the Sn_{Mg} defect is much lower than those of the others; thus, it is the defect with the highest concentration in MgSnN$_2$. As shown in Fig. 2(f), Sn_{Mg} does not introduce a localized defect state near the conduction-band maximum (CBM). Instead, it creates an occupied hydrogenic state, namely,

a perturbed host state, and acts as a shallow donor. As a result, Sn_{Mg} will generate unintentionally doped electron carriers and stabilize in the 2+ state. V_N and O_N are also found to be hydrogenic donors stabilized in the 1+ state. Their formation energies are higher than that of Sn_{Mg} but still lower than those of other defects. When the Fermi level is close to the CBM, Mg_{Sn} also has a relatively low formation energy in the 2− state. The defect states of Mg_{Sn} are quite localized, as seen in Fig. 2(g). In contrast to Sn_{Mg}, Mg_{Sn} acts as an acceptor with the ± and 1− or 2− transition levels located at 0.25 and 1.09 eV above the VBM, respectively. Therefore, Mg_{Sn} is the dominant acceptor that compensates for the electrons generated by the shallow donors Sn_{Mg}, V_N, and O_N. Except for these four types of defects, all other defects have quite high formation
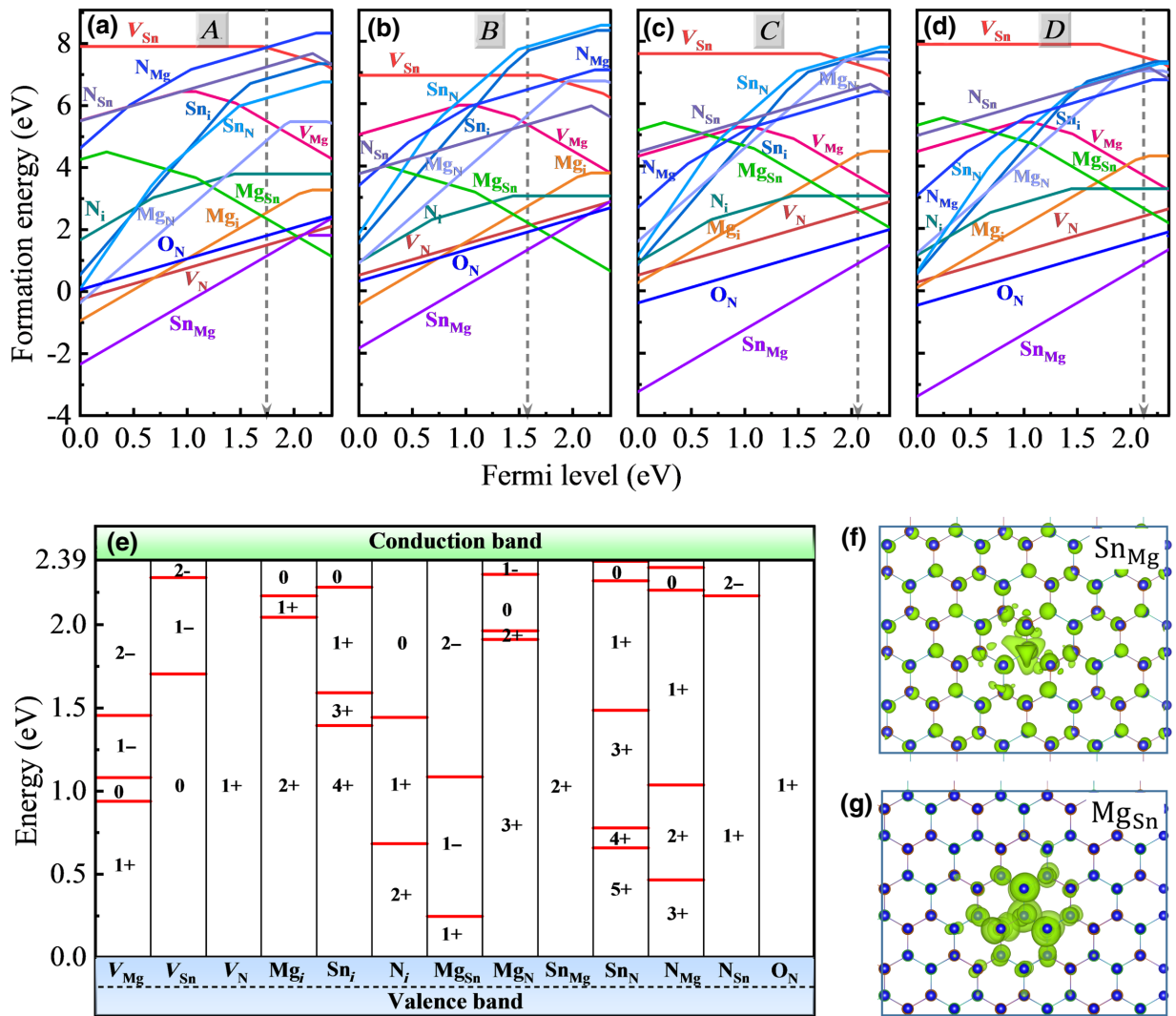

FIG. 2. Formation energies of native point defects and O_N impurities in MgSnN$_2$ as a function of Fermi level under chemical potential points (a) *A*, (b) *B*, (c) *C*, and (d) *D*, as labeled in Fig. 1(c). Gray arrows indicate the self-consistently calculated Fermi level. (e) Defect charge-state transition levels within the band gap of MgSnN$_2$. (f),(g) Charge-density distributions of donor and acceptor states for Sn_{Mg} and Mg_{Sn} under neutral states, respectively. Isosurface value is 0.0003 e/bohr^3.
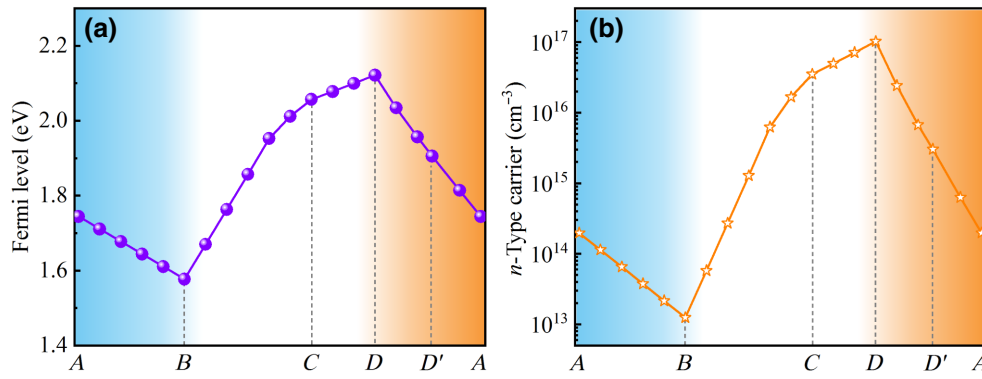
FIG. 3.   (a) Calculated Fermi levels (referenced to the VBM) and (b) electron concentrations in cation-ordered $MgSnN_2$ with native point defects and O_N impurities at a growth temperature of 700 K under different chemical potential conditions from points A to D.

energies, and their concentrations in $MgSnN_2$ should be quite low. Due to the higher formation energy of the Mg_{Sn} acceptor than that of the Sn_{Mg} donor, overall, $MgSnN_2$ will be unintentionally doped as an n-type material. The trends in the defect-formation energies observed here are consistent with those reported in previous studies [22].

Next, we quantitatively investigate the unintentionally doped electron concentration induced by the native defects and O_N impurities in cation-ordered $MgSnN_2$. Figure 3 shows the calculated Fermi levels and electron-carrier concentrations at 700 K with different chemical potentials, changing from A to D [Fig. 1(c)]. Since Sn_{Mg} is the dominant donor, the Fermi-level position and carrier concentration are strongly correlated to the formation energy of Sn_{Mg}. At points A and B, which correspond to the Mg-rich or moderate condition, the electron concentration is in the order of 10^{13}–10^{14} cm^{-3} due to the relatively high formation energy of Sn_{Mg}. When the growth environment become Sn rich and Mg poor, the formation energy of Sn_{Mg} is lowered, and the electron density increases significantly to 10^{16}–10^{17} cm^{-3}. Therefore, to reduce the concentration of unintentionally doped electrons in $MgSnN_2$, the Mg-rich and Sn-poor condition is preferred. Figure 3(b) also indicates that the maximum concentration of self-doped electrons is 1.02×10^{17} cm^{-3} in cation-ordered $MgSnN_2$, which is achieved at point D. Moreover, if one considers N_2 as the competing phase instead of the active-N source, the maximum concentration decreases to 10^{15} cm^{-3}, as achieved at point D' in Fig. 1(c). Hence, for cation-ordered $MgSnN_2$ with the wurtzitelike phase, one expects a moderate or low unintentional doping level, which meets the requirements for an optimal electron concentration for photovoltaic applications, where the electron concentration needs to be controlled at around 10^{16}–10^{18} cm^{-3} [21,22].

The conclusion that is reached above seems to be inconsistent with experimental observations, which show that $MgSnN_2$ samples have self-doped electron densities on the order of 10^{19}–10^{20} cm^{-3} [16,19]. The maximum

concentration of 1.02×10^{17} cm^{-3} calculated here is 3 orders of magnitude smaller than that obtained from experiments. Similar to our results, Han *et al.* also found that the calculated values of defect-induced electron densities in cation-ordered $MgSnN_2$ were 2–3 orders of magnitude lower than the experimentally measured values [22]. A possible origin of the discrepancy between calculations and experiments is the disorder in $MgSnN_2$. While the ground-state structures of II-IV-V2 compounds belong to the $Pna2_1$ space group, both experimental and theoretical studies confirm that there can be II-IV cation exchange in II-IV-V_2 compounds, leading to compositional disorder in the cation sublattice [5,26], and the degree of disorder depends on the growth conditions. Cation disorder can significantly affect the defect properties of $MgSnN_2$, as discussed in the next section.

C. Defects in cation-disordered $MgSnN_2$

Before exploring the effects of disorder on the defect properties, we first need to construct proper models of cation-disordered $MgSnN_2$. Since $MgSnN_2$ has a wurtzite-like structure, the cation sublattice can be approximated by a hexagonal-close-packed (HCP) lattice, and then the cation-disordered structures can be viewed as Mg-Sn alloys with a 1:1 ratio in the HCP lattice. The total energy of such a model can be described by the CE method [47–49]:

$$E(\sigma) = E_0 + \sum_{km} J_{km} \bar{\Pi}_{km},$$

where $E(\sigma)$ is the total energy of a structure with configuration σ, E_0 is a constant, J_{km} is the effective cluster interaction (ECI) of the cluster that consists of k atoms and is indexed by m, and $\bar{\Pi}_{km}$ is the averaged structural correlation function of that cluster. The fitted ECIs are given in Table S2 within the Supplemental Material [43]. With the CE Hamiltonian, we perform Metropolis MC simulations in a 432-atom supercell to generate cation-disordered structures of $MgSnN_2$. The degree of cation
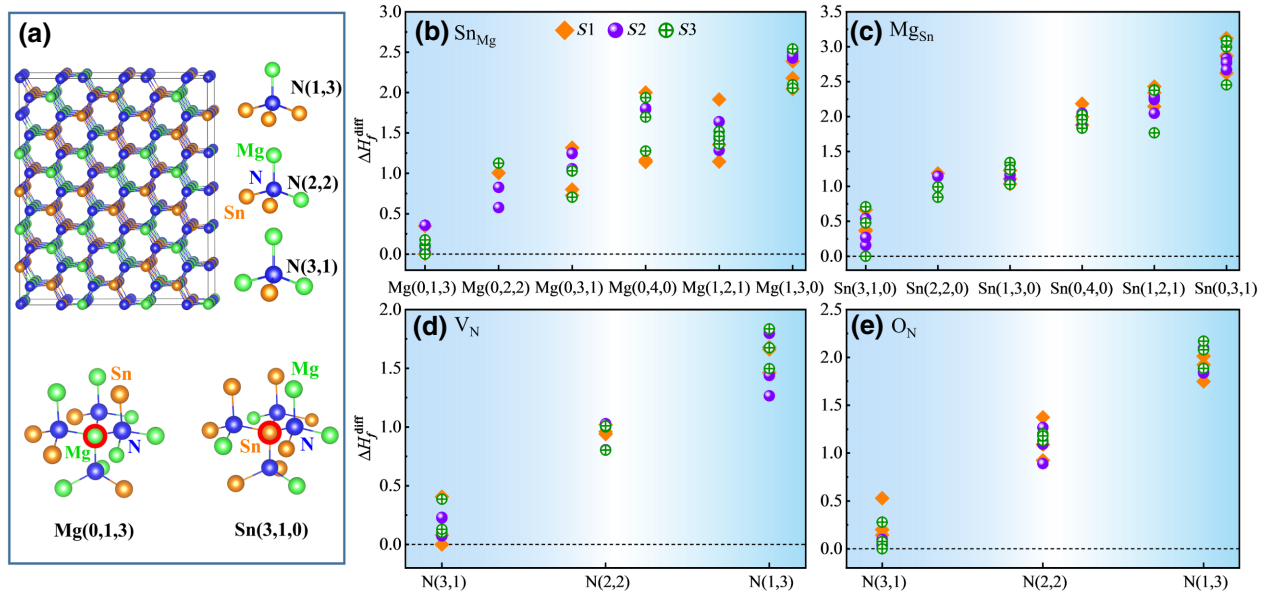
FIG. 4. (a) Example of cation-disordered MgSnN$_2$ structure generated from the MC simulation. Local environment of a nitrogen site is denoted as N(nMg, nSn), where nMg and nSn correspond to the numbers of Mg and Sn atoms in the tetrahedron. Each cation site is coordinated by four neighboring N atoms with different local environments. For example, Mg(0,1,3) represents the local environment of the Mg atom coordinated by one N(2,2) and three N(3,1) motifs, and Sn(3,1,0) represents the Sn atom coordinated by three N(1,3) and one N(2,2) motifs. Formation-energy difference, $\Delta H_f^{\mathrm{diff}}$, of the (b) Sn$_{\mathrm{Mg}}$, (c) Mg$_{\mathrm{Sn}}$, (d) V_{N}, and (e) O$_{\mathrm{N}}$ defects under different local environments in three host structures (S1, S2, and S3) picked from the MC calculations. $\Delta H_f^{\mathrm{diff}}$ is referenced to the lowest formation energy obtained among the considered defect sites. All the $\Delta H_f^{\mathrm{diff}}$ values are calculated using the HSE06 functional.

disorder, which varies with simulation temperature, can be described by an order parameter: x_{22}. x_{22} is defined as the fraction of nitrogen atoms that are coordinated by exactly two Mg atoms and two Sn atoms, since these atoms retain the local bonding environment in the ordered structure [26]. Previous studies demonstrated that the band gap of II-IV-V$_2$ compounds decreases as the degree of disorder increases (thus, x_{22} decreases) [5,26,50]. A recent experiment showed that, compared to the ordered structure, under typical growth conditions, the band gap of cation-disordered MgSnN$_2$ was reduced by approximately 0.5 eV [16]. Our MC simulations reveal that this is achieved with a value of x_{22} of about 0.9. Therefore, we use structures with values of around 0.9 for x_{22} as representatives of cation-disordered MgSnN$_2$. It is interesting to note that the band-gap reduction mostly comes from the energy increase of the VBM, whereas the energy decrease of the CBM has only a slight contribution. This can be understood by the localized nature and weak interatomic coupling of the N 2p driven VBM state, as indicated by the much smaller dispersion of valence bands than conduction bands [Fig. 1(b)]. These characteristics make the VBM energy more sensitive to local potential fluctuation induced by disorder.

In cation-disordered MgSnN$_2$, a given type of defect can have many different local environments. Thus, its formation energy, $\Delta H_f(\alpha, q, s)$, depends on defect site s. With a fixed cutoff radius, each site can be classified into a

particular local environment, β. As shown in Fig. 4(a), the local environment of a nitrogen site can be denoted as N(nMg, nSn), where n_{Mg} and n_{Sn} are the numbers of neighboring Mg and Sn atoms, respectively. For structures with a value of x_{22} [namely, the fraction of N(2,2)] of around 0.9 generated from our MC simulations, we find that the concentrations of N(0,4) and N(4,0) motifs are negligible due to their extremely high formation energies; this is in agreement with previous studies [26]. Therefore, we consider structures without N(0,4) and N(4,0). For a cation site, its local environment can be denoted as Mg($n_{\mathrm{N(1,3)}}$, $n_{\mathrm{N(2,2)}}$, $n_{\mathrm{N(3,1)}}$) or Sn($n_{\mathrm{N(1,3)}}$, $n_{\mathrm{N(2,2)}}$, $n_{\mathrm{N(3,1)}}$), where nN(1,3), nN(2,2), and nN(3,1) are the numbers of N(1,3), N(2,2), and N(3,1) sites in its nearest neighbor, respectively, as illustrated in Fig. 4(a). In Table S3 within the Supplemental Material [43], we show the average concentration of each local configuration by analyzing 55 cation-disordered structures with $x_{22} = 0.9$ obtained from our MC simulations. In the following, we consider only the local configurations with concentrations higher than 1%.

Next, we study the defects in disordered MgSnN$_2$. In the previous section, we show that Sn$_{\mathrm{Mg}}^{2+}$, V_{N}^{1+}, and O$_{\mathrm{N}}^{1+}$ are the major sources of n-type doping, whereas Mg$_{\mathrm{Sn}}^{2-}$ is the dominant compensating defect, so we consider these four types of defects in the following. The dependence of the defect-formation energy on the local environment is first examined. We randomly pick three
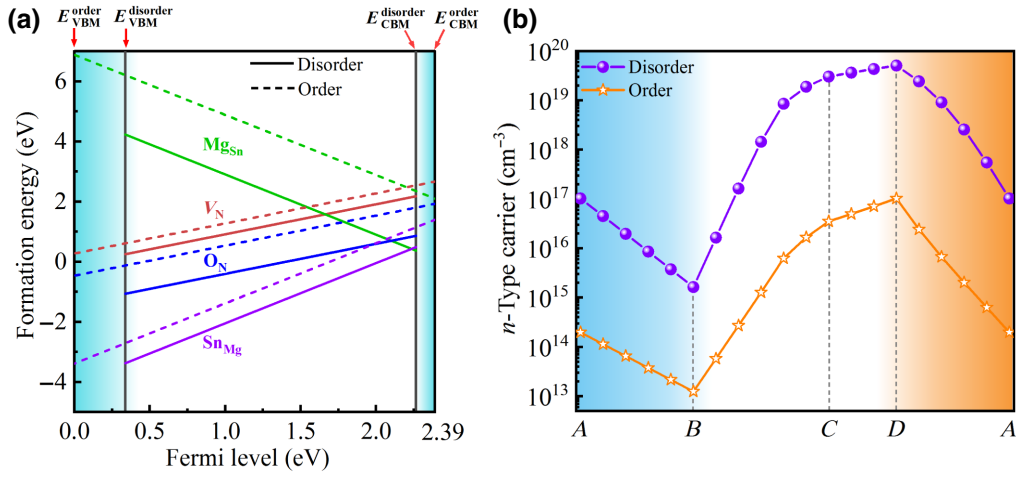
FIG. 5.   (a) Effective formation energies of Sn_{Mg}^{2+}, Mg_{Sn}^{2-}, V_N^{1+}, and O_N^{1+} as a function of Fermi level for cation-disordered and -ordered $MgSnN_2$ at chemical potential point D, calculated using the HSE06 method. Two gray solid vertical lines represent the average band-edge positions of cation-disordered $S1$, $S2$, and $S3$ $MgSnN_2$ structures. (b) Electron concentrations of cation-disordered and -ordered $MgSnN_2$ at a growth temperature of 700 K under different chemical potential conditions from points A to D.

structures ($S1$, $S2$, $S3$) with an order parameter of 0.9 from the MC simulation as host materials (see the Supplemental Material for their structures [43]) and calculate the total energy of the defective supercells with different local environments around the defect sites. We are interested in the relative formation-energy difference, ΔH_f^{diff}, for the same types of defects on lattice sites with different local environments. In Figs. 4(b)–4(e), the calculated values of ΔH_f^{diff} for Sn_{Mg}, Mg_{Sn}, V_N, and O_N are presented. Notably, ΔH_f^{diff} is referenced to the lowest formation energy obtained among the considered defect sites. It is seen that the formation energy strongly depends on the local environment. For defects with the same local environment, the discrepancy in formation energy is typically around 0.5 eV. When the local environment differs, the formation-energy difference can be 2–3 eV. For each type of defect, there is an energetically favorable local environment, β_0. For example, for Sn_{Mg}, the Sn atom prefers to substitute the Mg(0,1,3) sites. This can be attributed to the local environment change after Sn substitution. In the vicinity of a Mg(0,1,3) site, there are three N(3,1) and one N(2,2) motifs. When a Sn atom replaces the Mg atom, the configuration becomes three N(2,2) and one N(1,3) motifs. Compared to the N(2,2) motif, the N(1,3) and N(3,1) motifs have higher energy [26]. The increased number of the N(2,2) motifs after the formation of Sn_{Mg} at a Mg(0,1,3) site largely restores the local environment in ordered $MgSnN_2$, leading to a significant energy gain and a reduction in the defect-formation energy. For the same reason, the Mg_{Sn} defect prefers to occur at the Sn(3,1,0) sites. For V_N and O_N, the N(3,1) site has the lowest formation energy. This is understood from the perspective of the Coulomb energy. Because Mg has a chemical valence of +2, while that of Sn is +4, the Coulomb repulsion energy felt by a +1 charged donor will

be smaller when there are more Mg atoms in its nearest neighbor.

In disordered materials, in general, one can define an effective formation energy, $\Delta H_{eff}(\alpha, q, T)$, as [51]

$$\exp\left[\frac{-\Delta H_{eff}(\alpha, q, T)}{k_B T}\right] = \frac{1}{N_{site}} \sum_s \exp\left[\frac{-\Delta H_f(\alpha, q, s)}{k_B T}\right].$$

According to Fig. 4, for defect sites s, belonging to most-favored local environment β_0, all the defect-formation energies have similar magnitudes, the mean value of which, $\Delta\bar{H}_f(\alpha, q, \beta_0)$, is significantly smaller than the formation energies of other configurations. Hence, the summation in the above equation is dominated by $s \in \beta_0$ and we have

$$\exp\left[\frac{-\Delta H_{eff}(\alpha, q, T)}{k_B T}\right] = \frac{1}{N_{site}} \sum_s exp\left[\frac{-\Delta H_f(\alpha, q, s)}{k_B T}\right],$$

$$\approx \frac{1}{N_{site}} \sum_{s \in \beta_0} exp\left[\frac{-\Delta H_f(\alpha, q, s)}{k_B T}\right],$$

$$\approx \frac{N_{\beta_0}}{N_{site}} exp\left[\frac{-\Delta\bar{H}_f(\alpha, q, \beta_0)}{k_B T}\right].$$

Here, N_{β_0}/N_{site} is the concentration of defect sites that belong to β_0. Notably, we have $(N_{\beta_0}/N_{site}) > 1\%$ for all the defects considered. In Fig. 5(a), we plot the HSE06-calculated $\Delta H_{eff}(\alpha, q, T)$ at $T = 700$ K. It can be observed that, compared with cation-ordered $MgSnN_2$, the effective formation energies of the dominant defects in cation-disordered $MgSnN_2$ are greatly reduced. Similar to the case of the ordered structure, Sn_{Mg} has the lowest formation energy in structures with cation disorder. Using

$\Delta H_{\text{eff}}(\alpha, q, T)$ and the average band-edge positions of $S1$, $S2$, and $S3$, we calculate the equilibrium carrier concentration contributed to by these dominant defects, as seen in Fig. 5(b). When the chemical potential is located at point D in Fig. 5(b), the electron concentration is 5.08×10^{19} cm^{-3}, which is increased by over 2 orders of magnitude compared to that of cation-ordered MgSnN$_2$. Besides the reduced defect-formation energy, the slightly lowered CBM position in cation-disordered MgSnN$_2$ [Fig. 5(a)] can also contribute to the increased electron concentration. Experimentally, it is observed that the unintentional n-type doping level is 10^{19}–10^{20} cm^{-3} [16,19], which is in good agreement with our calculations. Therefore, we propose that the Sn$_{\text{Mg}}$ antisite defect in the cation-disordered phase is responsible for the very high unintentional n-type conductivity observed in experiments. To reduce the concentration of unintentionally doped electrons, it would be beneficial to decrease the degree of cation disorder in MgSnN$_2$.

IV. CONCLUSION

We study the native point defects and oxygen impurities in cation-ordered and -disordered MgSnN$_2$ by performing first-principles hybrid-functional calculations. The results show that Sn$_{\text{Mg}}$ is the predominant donor defect, contributing to an electron concentration as high as 10^{17} cm^{-3} in cation-ordered MgSnN$_2$ under Sn-rich or Mg-poor conditions. The level of unintentional doping can be further decreased under Sn-poor conditions. The results indicate that, if MgSnN$_2$ samples can be grown with a high crystal quality, they can meet the requirements for photovoltaic applications, where the electron concentration needs to be controlled at around 10^{16}–10^{18} cm^{-3}. The cation disorder in MgSnN$_2$ greatly influences the electron concentration. It is found that cation disorder significantly decreases the formation energies of dominant defects, such as Sn$_{\text{Mg}}$, leading to a much higher self-doped electron concentration (10^{19} cm^{-3}) than in the case of the cation-ordered phase. The reduced formation energy can be understood by the energy gain due to the creation of energetically favorable local motif structures after the formation of defects. Hence, such cation-disorder-enhanced unintentional doping could be a possible origin of the high electron-carrier density (10^{19}–10^{20} cm^{-3}) of MgSnN$_2$ observed in experiments. Decreasing the degree of cation disorder is beneficial for reducing the densities of defects and self-doped carriers. Our work thus provides insights into the defect properties in compositionally disordered materials and could be helpful for carrier control in MgSnN$_2$ samples and their applications in electronic devices.

[1] M. Razeghi, III-Nitride optoelectronic devices: From ultraviolet toward terahertz, IEEE Photonics J. **3**, 263 (2011).

[2] J. Hu, Y. Zhang, M. Sun, D. Piedra, N. Chowdhury, and T. Palacios, Materials and processing issues in vertical GaN power electronics, Mater. Sci. Semicond. Process. **78**, 75 (2018).

[3] L. J. Lin and Y. P. Chiou, Optical design of GaN/In$_x$Ga$_{1-x}$N/cSi tandem solar cells with triangular diffraction grating, Opt. Express **23**, A614 (2015).

[4] F. Kawamura, H. Murata, M. Imura, N. Yamada, and T. Taniguchi, Synthesis of CaSnN$_2$ via a high-pressure metathesis reaction and the properties of II-Sn-N$_2$ (II = Ca, Mg, Zn) semiconductors, Inorg. Chem. **60**, 1773 (2021).

[5] R. A. Makin, K. York, S. M. Durbin, N. Senabulya, J. Mathis, R. Clarke, N. Feldberg, P. Miska, C. M. Jones, Z. Deng, L. Williams, E. Kioupakis, and R. J. Reeves, Alloy-Free Band Gap Tuning across the Visible Spectrum, Phys. Rev. Lett. **122**, 256403 (2019).

[6] T. Hamaguchi, H. Nakajima, M. Tanaka, M. Ito, M. Ohara, T. Jyoukawa, N. Kobayashi, T. Matou, K. Hayashi, H. Watanabe, R. Koda, and K. Yanashima, Sub-milliampere-threshold continuous wave operation of GaN-based vertical-cavity surface-emitting laser with lateral optical confinement by curved mirror, Appl. Phys. Express **12**, 044004 (2019).

[7] F. Alnjiman, A. Virfeu, D. Pilloud, S. Diliberto, E. Haye, A. E. Giba, S. Migot, J. Ghanbaja, P. Boulet, H. Albrithen, and J.-F. Pierson, Theoretical and experimental approaches for the determination of functional properties of MgSnN$_2$ thin films, Sol. Energy Mater. Sol. Cells **244**, 111797 (2022).

[8] A. Even, G. Laval, O. Ledoux, P. Ferret, D. Sotta, E. Guiot, F. Levy, I. C. Robin, and A. Dussaigne, Enhanced In incorporation in full InGaN heterostructure grown on relaxed InGaN pseudo-substrate, Appl. Phys. Lett. **110**, 262103 (2017).

[9] M. Kute, Z. Deng, S. Chae, and E. Kioupakis, Cation-size mismatch as a predictive descriptor for structural distortion, configurational disorder, and valence-band splitting in II-IV-N$_2$ semiconductors, Appl. Phys. Lett. **119**, 132104 (2021).

[10] A. D. Martinez, A. N. Fioretti, E. S. Toberer, and A. C. Tamboli, Synthesis, structure, and optoelectronic properties of II-IV-V$_2$ materials, J. Mater. Chem. A **5**, 11418 (2017).

[11] R. R. Schnepf, J. J. Cordell, M. B. Tellekamp, C. L. Melamed, A. L. Greenaway, A. Mis, G. L. Brennecka, S. Christensen, G. J. Tucker, E. S. Toberer, S. Lany, and A. C. Tamboli, Utilizing site disorder in the development of new energy-relevant semiconductors, ACS Energy Lett. **5**, 2027 (2020).

[12] N. L. Adamski, Z. Zhu, D. Wickramaratne, and C. G. Van de Walle, Optimizing *n*-type doping of ZnGeN$_2$ and ZnSiN$_2$, Phys. Rev. B **100**, 155206 (2019).

[13] S. Chen, P. Narang, H. A. Atwater, and L. W. Wang, Phase stability and defect physics of a ternary ZnSnN$_2$ semiconductor: First principles insights, Adv. Mater. **26**, 311 (2014).

[14] A. Zakutayev, S. R. Bauers, and S. Lany, Experimental synthesis of theoretically predicted multivalent ternary nitride materials, Chem. Mater. **34**, 1418 (2022).

[15] A. L. Greenaway, C. L. Melamed, M. B. Tellekamp, R. Woods-Robinson, E. S. Toberer, J. R. Neilson, and A. C. Tamboli, Ternary nitride materials: Fundamentals and emerging device applications, Annu. Rev. Mater. Res. **51**, 591 (2021).

[16] A. L. Greenaway, A. L. Loutris, K. N. Heinselman, C. L. Melamed, R. R. Schnepf, M. B. Tellekamp, R. Woods-Robinson, R. Sherbondy, D. Bardgett, S. Bauers, A. Zakutayev, S. T. Christensen, S. Lany, and A. C. Tamboli, Combinatorial synthesis of magnesium tin nitride semiconductors, J. Am. Chem. Soc. **142**, 8421 (2020).

[17] N. Yamada, M. Mizutani, K. Matsuura, M. Imura, H. Murata, J. Jia, and F. Kawamura, Band gap-tunable (Mg, Zn)SnN$_2$ earth-abundant alloys with a wurtzite structure, ACS Appl. Energy Mater. **3**, 4934 (2021).

[18] F. Kawamura, M. Imura, H. Murata, N. Yamada, and T. Taniguchi, Synthesis of a novel rocksalt-type ternary nitride semiconductor MgSnN$_2$ using the metathesis reaction under high pressure, Eur. J. Inorg. Chem. **2020**, 446 (2019).

[19] N. Yamada, K. Matsuura, M. Imura, H. Murata, and F. Kawamura, Composition-dependent properties of wurtzite-type Mg$_{1+x}$Sn$_{1-x}$N$_2$ epitaxially grown on GaN(001) templates, ACS Appl. Energy Mater. **3**, 1341 (2021).

[20] S. Yata, M. Mizutani, K. Makiuchi, F. Kawamura, M. Imura, H. Murata, J. Jia, and N. Yamada, Electron transport properties in degenerate magnesium tin oxynitride (Mg$_{1-x}$Sn$_{1+x}$N$_{2-2y}$O$_{2y}$) with average wurtzite structure, J. Appl. Phys. **131**, 075302 (2022).

[21] N. Tsunoda, Y. Kumagai, A. Takahashi, and F. Oba, Electrically Benign Defect Behavior in Zinc Tin Nitride Revealed from First Principles, Phys. Rev. Appl. **10**, 011001 (2018).

[22] D. Han, S. S. Rudel, W. Schnick, and H. Ebert, Self-doping behavior and cation disorder in MgSnN$_2$, Phys. Rev. B **105**, 125202 (2022).

[23] L. Lahourcade, N. C. Coronel, K. T. Delaney, S. K. Shukla, N. A. Spaldin, and H. A. Atwater, Structural and optoelectronic characterization of rf sputtered ZnSnN$_2$, Adv. Mater. **25**, 2562 (2013).

[24] E. Burstein, Anomalous optical absorption limit in InSb, Phys. Rev. **93**, 632 (1954).

[25] D. Skachkov, P. C. Quayle, K. Kash, and W. R. L. Lambrecht, Disorder effects on the band structure of ZnGeN$_2$: Role of exchange defects, Phys. Rev. B **94**, 205201 (2016).

[26] S. Lany, A. N. Fioretti, P. P. Zawadzki, L. T. Schelhas, E. S. Toberer, A. Zakutayev, and A. C. Tamboli, Monte Carlo simulations of disorder in ZnSnN$_2$ and the effects on the electronic structure, Phys. Rev. Mater. **1**, 035401 (2017).

[27] T. D. Veal, N. Feldberg, N. F. Quackenbush, W. M. Linhart, D. O. Scanlon, L. F. J. Piper, and S. M. Durbin, Band gap dependence on cation disorder in ZnSnN$_2$ solar absorber, Adv. Energy Mater. **5**, 1501462 (2015).

[28] X. Zhang, J. Kang, and S.-H. Wei, Defect modeling and control in structurally and compositionally complex materials, Nat. Comput. Sci. **3**, 210 (2023).

[29] W. Chen, D. Dahliah, G.-M. Rignanese, and G. Hautier, Origin of the low conversion efficiency in Cu$_2$ZnSnS$_4$ kesterite solar cells: The actual role of cation disorder, Energy Environ. Sci. **14**, 3567 (2021).

[30] G. Kresse and J. Furthmüller, Efficient iterative schemes for *ab initio* total-energy calculations using a plane-wave basis set, Phys. Rev. B **54**, 11169 (1996).

[31] B. Adolph, J. Furthmüller, and F. Bechstedt, Optical properties of semiconductors using projector-augmented waves, Phys. Rev. B **63**, 125108 (2001).

[32] G. Kresse and D. Joubert, From ultrasoft pseudopotentials to the projector augmented-wave method, Phys. Rev. B **59**, 1758 (1999).

[33] J. P. Perdew, K. Burke, and M. Ernzerhof, Generalized Gradient Approximation Made Simple, Phys. Rev. Lett. **77**, 3865 (1996).

[34] A. V. Krukau, O. A. Vydrov, A. F. Izmaylov, and G. E. Scuseria, Influence of the exchange screening parameter on the performance of screened hybrid functionals, J. Chem. Phys. **125**, 224106 (2006).

[35] J. D. Pack and H. J. Monkhorst, Special points for Brillouin-zone integrations—a reply, Phys. Rev. B **16**, 1748 (1977).

[36] Y. Kumagai, M. Choi, Y. Nose, and F. Oba, First-principles study of point defects in chalcopyrite ZnSnP$_2$, Phys. Rev. B **90**, 125202 (2014).

[37] C. Freysoldt, J. Neugebauer, and C. G. Van de Walle, Fully *Ab Initio* Finite-Size Corrections for Charged-Defect Supercell Calculations, Phys. Rev. Lett. **102**, 016402 (2009).

[38] C. Freysoldt, J. Neugebauer, and C. G. Van de Walle, Electrostatic interactions between charged defects in supercells, Phys. Status Solidi B **248**, 1067 (2011).

[39] S. Lany and A. Zunger, Assessment of correction methods for the band-gap problem and for finite-size effects in supercell defect calculations: Case studies for ZnO and GaAs, Phys. Rev. B **78**, 235104 (2008).

[40] J. H. Yang, W. J. Yin, J. S. Park, and S. H. Wei, Self-regulation of charged defect compensation and formation energy pinning in semiconductors, Sci. Rep. **5**, 16977 (2015).

[41] J. Buckeridge, Equilibrium point defect and charge carrier concentrations in a material determined through calculation of the self-consistent Fermi energy, Comput. Phys. Commun. **244**, 329 (2019).

[42] A. van de Walle, M. Asta, and G. Ceder, The alloy theoretic automated toolkit: A user guide, Calphad **26**, 539 (2002).

[43] See the Supplemental Material at http://link.aps.org/supplemental/10.1103/PhysRevApplied.19.054046 for the bulk properties of MgSnN$_2$, the cluster expansion Hamiltonian construction, and details of Monte Carlo simulations. References [16,22,26,47–49] are also included in the Supplemental Material.

[44] S. Lyu and W. R. L. Lambrecht, Quasiparticle self-consistent *GW* band structures of Mg-IV-N$_2$ compounds: The role of semicore *d* states, Solid State Commun. **299**, 113664 (2019).

[45] P. Kroll, T. Schröter, and M. Peters, Prediction of novel phases of tantalum(V) nitride and tungsten(VI) nitride that

can be synthesized under high pressure and high temperature, Angew. Chem., Int. Ed. **44**, 4249 (2005).

[46] W. Sun, A. Holder, B. Orvañanos, E. Arca, A. Zakutayev, S. Lany, and G. Ceder, Thermodynamic routes to novel metastable nitrogen-rich nitrides, Chem. Mater. **29**, 6936 (2017).

[47] J. M. Sanchez, F. Ducastelle, and D. Gratias, Generalized cluster description of multicomponent systems, Phys. A **128**, 334 (1984).

[48] D. B. Laks, L. G. Ferreira, S. Froyen, and A. Zunger, Efficient cluster expansion for substitutional systems, Phys. Rev. B **46**, 12587 (1992).

[49] J. Yang, P. Zhang, and S. H. Wei, Band structure engineering of $Cs_2AgBiBr_6$ perovskite through order-disordered transition: A first-principle study, J. Phys. Chem. Lett. **9**, 31 (2018).

[50] R. A. Makin, K. York, S. M. Durbin, and R. J. Reeves, Revisiting semiconductor band gaps through structural motifs: An Ising model perspective, Phys. Rev. B **102**, 115202 (2020).

[51] J. Yang and S.-H. Wei, First-principles study of the band gap tuning and doping control in $CdSe_xTe_{1-x}$ alloy for high efficiency solar cell, Chin. Phys. B **28**, 086106 (2019).